Laser-Induced Forward Transfer (LIFT) Process for Flexible Construction of Advanced 3D Silicon Anode Designs in High-Energy Lithium-Ion Batteries

U. Rist[*], Y. Sterzl, W. Pfleging

Karlsruhe Institute of Technology, IAM-AWP, P.O. Box 3640, 76021 Karlsruhe, Germany

ABSTRACT

The demand for optimized and affordable lithium-ion battery systems increases with the growing number of electrified vehicles. To this aim, 3D electrode architectures and new high energy density materials like silicon are in the focus of research. To implement silicon in the LIFT-process for fast prototype development, a silicon-rich paste was developed and optimized for the printing. The electrodes containing the silicon-rich paste showed a rather high specific capacity of $3029 \, mAh \cdot g^{-1}$. To achieve an enhanced cyclability, a new electrode architecture was developed by using subtractive and additive laser processing in a process chain. For this purpose, a state-of-the-art coated graphite electrode was structured, and the cavities were subsequently partially filled with the silicon-rich paste. After reaching end-of-life, the coin cells were disassembled and analyzed using SEM and LIBS measurements regarding the failure mechanisms.

Keywords: LIFT, anode printing, ablation, lithium-ion battery, 3D battery, multilayer anode, silicon, graphite

1. INTRODUCTION

The growing number of electrified vehicles increases the demand for affordable, reliable, and optimized lithium-ion batteries with fast charging capabilities. Adapted materials and electrode geometries are necessary to achieve the next level of development [1–5]. Hereby, silicon is considered as next generation active anode material due to its one order of magnitude higher specific energy density compared to the so far commonly used graphite material [6]. During lithiation, i.e., battery charging, silicon undergoes enormous volume expansion, which leads to mechanical degradation and thus rapid capacity fading [7]. The realization of 3D lithium-ion batteries by laser-assisted patterning of electrodes presents a novel technological approach addressing the rapid degradation of silicon electrodes by creation of artificial porosities within the composite electrode.The additional porosity is essential for enabling almost defect-free silicon expansion during lithiation [1, 2]. As stand-alone technology or in addition to laser direct ablation, printing technologies offer a versatile procedure for the development of advanced 3D electrode designs adapted to application scenarios. In research, LIFT was already applied for LCO ($LiCoO_2$) micro batteries [8], for NMC ($LiNi_{1/3}Mn_{1/3}Co_{1/3}O_2$) cathodes which were subsequently laser structured [9], for graphite anodes [10, 11] and silicon containing multilayer anodes in coin cells [12]. In those studies, the used binder was polyvinylidene difluoride (PVDF) which is, due to weak surface interactions, not suitable for silicon containing electrodes [5, 13–15]. Therefore, at first, a silicon-rich paste or ink must be developed and analyzed. For this purpose, a silicon-rich paste is prepared using polyacrylic acid (PAA), which is a more suitable binder for silicon containing electrodes [13, 16, 17]. To increase the cycle lifetime of silicon containing electrodes, a 3D architecture was developed. A conventional-type composite graphite electrode was used as base material. Subsequently, grooves with a width of $100 \, \mu m$ were generated and afterwards, the silicon-rich paste was printed into the grooves applying LIFT. The developed electrodes were assembled in coin cells and electrochemically analyzed with C-rates up to 5C, followed by a lifetime study applying a C-rate of C/2. After reaching end-of-life, the batteries were disassembled, and the electrodes were characterized post mortem with scanning electron microscopy (SEM) and laser-induced breakdown spectroscopy (LIBS) to explore failure mechanisms.

*ulrich.rist@kit.edu; phone: +49 721 608 28161

2. EXPERIMENTAL SET-UP

The LIFT process for printing anodes is schematically displayed in Figure 1. As laser source a frequency tripled Nd:YAG laser (Lumentum, USA, Model: Q301-HD-1000R) was used with a pulse length of 78 ns and an operating wavelength of 355 nm. The laser provides a maximum average power of 10 W and a maximum repetition rate of 30 kHz. The gaussian shaped laser intensity profile is transformed to an 2D top-hat one by applying a diffractive optical element (DOE), as shown in Figure 1. The cross-sectional shape of the laser profile can be adjusted by a mask selector. Finally, the illuminated mask is projected via an objective lens on the paste with a demagnification factor of 3.5. With the mask selector, different motifs such as round or rectangular shaped ones can be selected. However, for large-areal printing the raw beam of the laser was used leading to a square shape with a side length of 175 µm at electrode paste. In contrast, for the positioned printing a square mask is selected leading to a side length of 47 µm. The printing paste is coated with a doctor blade onto a round quartz glass wafer (DSP-200×0675-SGQ-00, Wafer Universe, Germany) with a diameter of 200 mm large and a thickness of 0.675 mm. For the large-areal printing the anode paste was coated with a thickness of 40 µm onto the glass plate. Due to the smaller laser beam for positioned printing a higher energy density and a thinner paste thickness of about 20 µm is required for a voxel transfer [10]. In opposite to the quartz glass plate a 9 µm thick copper foil is placed for anode printing.
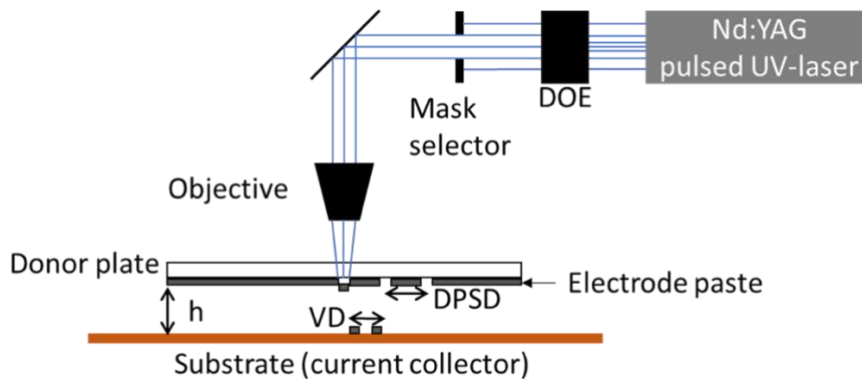

Figure 1: Schematic illustration of LIFT-process.

In this study, the LIFT process is in principle based on the fluid printing method described by Fernández-Pradas [18]. Hereby, material from the printing paste ("ink") is partially sublimated at the interface of the donor plate and printing paste. The resulting material vapor expands between the quartz glass wafer and the paste, removing a material cluster from ink and transferring it as a voxel to the substrate.

The manufacturing process of the customized electrode is schematically displayed in Figure 2. Here, subtractive and additive laser processes were used for the manufacturing of the new electrode design, in the following called SaA-electrode. For this purpose, a conventional coated composite graphite electrode is used as the basis material. A groove pattern with a groove width of 100 µm was structured using a laser with a wavelength of 1030 nm and a pulse duration of 600 fs. For a single groove, three ablation scans were performed using a hatch of 24 µm. Subsequently, silicon-rich paste was printed via LIFT in the created grooves. Due to the fact, that silicon undergoes significant volume expansion during lithiation, the cavities were only partially filled with silicon paste to allow for expansion. For the electrode in this study the groove-to-grove distance was set to 1 mm and 10 cycles of printing were performed for each groove.
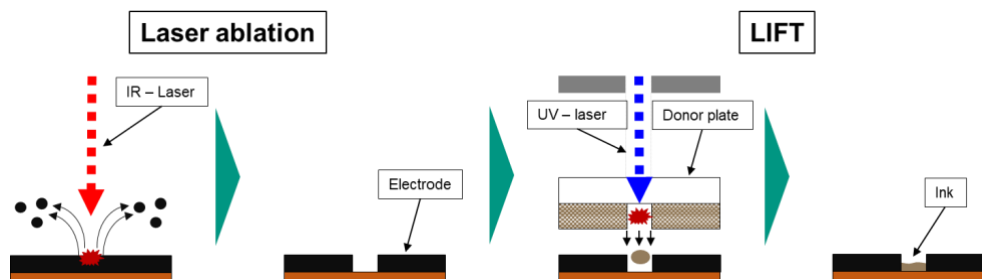

Figure 2: Schematic representation of the process sequence for producing the customized electrode architecture.

For the customized electrode, the graphite slurry for the conventional graphite anode is based on the recipe of J. Kumberg et. al. [19] which contains 93 wt.% flake-like graphite (T808, Targray, Canada) as active material. The graphite particles have a $d_{50} = 4.9$ µm, measured by laser scattering (LA-950, Horiba, Kyoto, Japan). To enhance the electric conductivity of the electrode layer, 1.4 wt.% carbon black (Super C65, Timcal, Swiss) was added. The binder system consists of 1.87 wt.% sodium carboxymethyl cellulose (Na-CMC) and 3.73 wt.% styrene-butadiene rubber (SBR). The material was dissolved in deionized water. The printing paste containing silicon is composed of 40 wt.% silicon (SI-15008, Targray, Canada, $d_{50} = 72$ nm) as the active material. To increase the electric conductivity of the silicon paste, 40 wt.% of carbon black was added to the Si based slurry. As a binder, 20 wt.% PAA (181285, Merck, Germany) was used. All components were dissolved in a 1:1 ratio mixture of water and glycerol. Glycerol was added to the printing paste as a solvent to ensure a sufficiently long printing time.

The printed electrodes were dried under vacuum at 80 °C for at least 12 h. They were then cut out using a 400 fs laser operating at a wavelength of 515 nm and dried again under the same conditions before being transferred into an argon-filled glovebox. The electrodes were assembled in CR2032 coin cells against lithium, followed by an electrochemical characterization using an Arbin system (BT 2000, Arbin Instruments, College Station, TX, USA). The cells were initially discharged at a constant current (CC) to a cut-off voltage of 0.01 V. Then, a constant voltage (CV) was applied until the cut-off current was reached (Table 1 & Table 2). The charging process involves only a constant current (CC) up to a cut-off voltage of 1.5 V. The C-rates represent the currents required to charge or discharge the battery within defined time frames. For electrochemical analysis, the cells were charged or discharge with different C-rates to analyze their charging/discharging behavior. For cells with silicon-rich electrodes, the priming cycling protocol consisted of a single C/50 cycle and three subsequent C/20 cycles. The batteries were cycled 50 times at C/10 and then three times at C/20, as shown in Table 1. The capacity retention (CR) of the batteries is calculated by dividing the discharge capacity of the last C/20 cycles by the priming capacity.

Table 1: Cycling protocol of batteries containing electrodes printed with only silicon-rich paste.

Discharging current	C/50	C/20	C/10	C/20
Charging current	C/50	C/20	C/10	C/20
Cut-off current	C/100	C/50	C/20	C/50
Cycle numbers	1	3	50	3

The batteries with the SaA-electrodes were primed with the same protocol as the batteries containing the electrodes with the silicon-rich slurry. Subsequently, rate capability analyses were applied by discharging the batteries, i.e., lithiation of the SaA-electrode, with currents up to 5C (Table 2). Then, a lifetime analysis was applied with 50 C/2 cycles, followed by 5 C/5 cycles as a control of cell degradation. The capacity retention of the batteries containing the SaA-electrodes is calculated by dividing the discharge capacity of the C/5 cycles with the discharge capacity of the C/5 cycles.

Table 2: Cycling protocol for batteries containing SaA-electrodes (rate capability analysis)

Discharging current	C/50	C/20	C/10	C/5	C/2	1C	2C	3C	5C	C/5
Charging current	C/50	C/20	C/10	C/5	C/5	C/5	C/5	C/5	C/5	C/5
Cut-off current	C/100	C/50	C/20	C/10	C/10	C/10	C/10	C/10	C/10	C/10
Cycle numbers	1	3	5	5	5	5	5	5	5	5

At the end-of-life (EoL) the cells were transferred in an argon-filled glovebox and disassembled. To remove the electrolyte, the electrodes were each washed for 30 minutes by placing them in two different jars filled with dimethyl carbonate (DMC). The electrodes were investigated post mortem by scanning electron microscopy (SEM, PW-100-018, Phenom-World BV, Eindhoven, The Netherlands). In addition to the cycled electrodes, also parts of the freshly electrode was examined as reference.

Furthermore, the electrodes from cycled and disassembled cells were analyzed using laser-induced breakdown spectroscopy (LIBS, FiberLIBS SN013, Secopta Analytics GmbH, Germany).

3. RESULTS AND DISCUSSION

Electrochemical analyses

To increase the specific capacity of anodes, silicon as active material is used in lithium-ion batteries. Here, the material as well as optimized electrode architecture were under investigation [2, 4, 20–23]. The electrochemical properties of the silicon-rich paste optimized for the LIFT process were first investigated in this study. For this purpose, first electrodes with the silicon-rich paste were printed, assembled in coin cells and electrochemically analyzed for 50 cycles. The corresponding results are displayed in Figure 3.
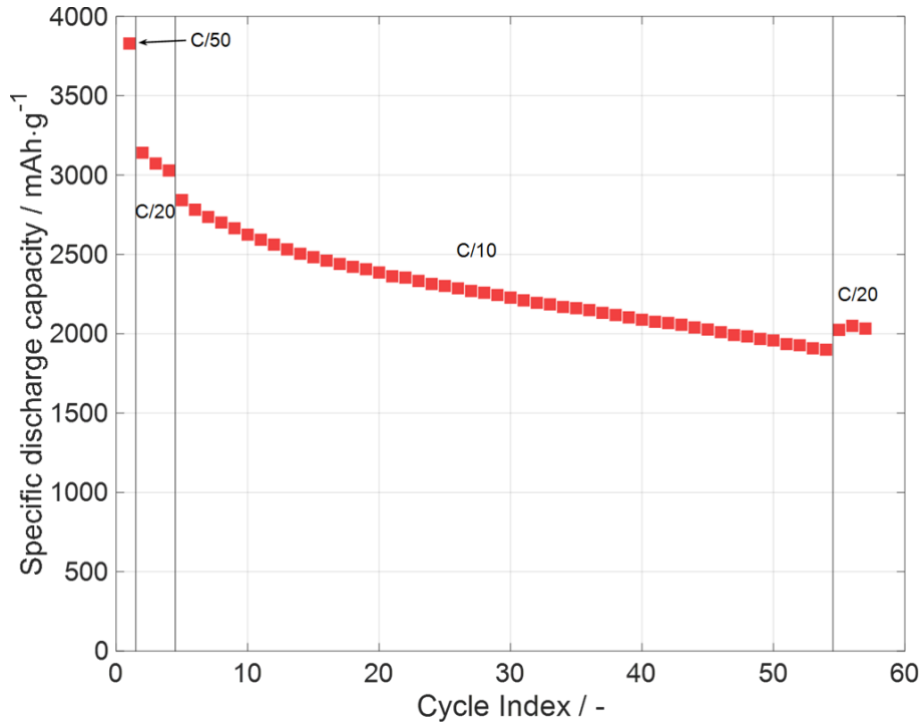

Figure 3: Long-term analysis of a battery with only silicon-rich slurry printed electrode for 50 C/10 cycles (CR at C/20: 66 %).

In Figure 3, the specific discharge capacity is displayed over the cycle index. It can be seen that at the end of the priming process the battery achieves a specific discharge capacity of 3029 mAh·g^{-1} which is nearby the theoretical capacity of pure silicon anodes (3579 mAh·g^{-1}). However, a silicon anode often falls short of achieving its theoretical capacity in battery tests due to the limited diffusion rate of lithium-ions within the silicon. This creates a kinetic barrier that prevents full conversion of silicon into $Li_{15}Si_4$ at a normal charge/discharge rate. Already at a C-rate of C/10 capacity fading can be observed. At the end of the lifetime analysis three C/20 cycles were applied to control the remaining capacity. Here, a capacity retention (CR) of 66 % is calculated. For conventional batteries a CR of 66 % at small currents of C/10 indicates low cyclability. However, it can be concluded that the initially specific capacity is quite high and that the battery with the silicon-rich 2D electrode shows an expected low cyclability. This motivates the development of a new electrode architecture to enhance the cyclability of silicon containing next generation anodes.

For this purpose, the new electrode architecture, as described and displayed earlier (Figure 2) was developed. In research, silicon-graphite blend electrodes have often been analyzed thus far [2, 6, 16, 24–26]. This work presents a new electrode design: a graphite-silicon electrode with separate and vertically aligned areas. The areas with the different active materials were separated so that there is less interaction of each other during cycling. With the graphite regions, the electrode has areas with good cyclability. The vertical arrangement was chosen so that the segmented areas are directly opposite to the counter electrode without coverage by other active materials. Furthermore, by only partially filling the laser generated grooves, the silicon can be given additional space to expand during lithiation. Since the printed Si composite material adheres to both the stable graphite region and the current collector, it is expected that the overall adhesion of the silicon region can be increased as a whole.

The SaA-electrodes were manufactured with a groove-to-groove distance ("pitch") of 1 mm and a groove width of 100 µm. The results of the electrochemical analysis are displayed in Figure 4. Determining the transferred amount is difficult due to slight differences in weight before and after printing, as well as unevenness in the composite graphite base material. For the displayed data the amount of silicon was calculated with the knowledge of the specific capacities of the different active materials and the material mass fraction in the separated areas. The overall amount of silicon was calculated to be 5.7 wt.%.
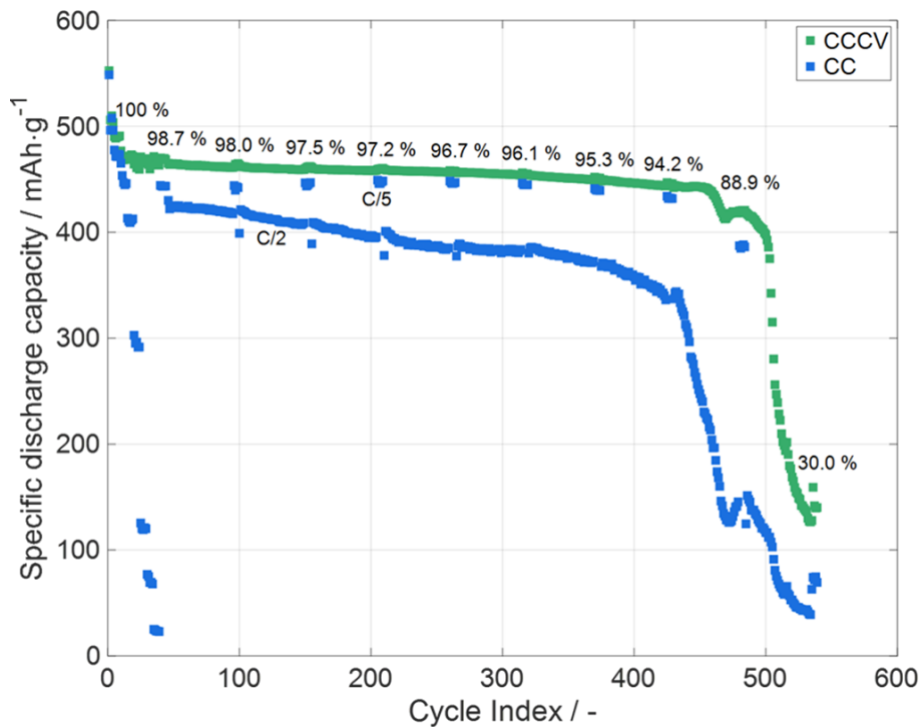

Figure 4: Electrochemical characterization of the SaA-electrode with a rate capability analysis and a subsequent long-term analysis with 5 C/5 cycles and 50 C/2 cycles, respectively. Implemented in the diagram are the CR values calculated by comparing the capacity of each C/5 cycle with the capacity of the first C/5 cycle. Calculated silicon content: 5.7 wt.%.

First the battery with the SaA-electrode is characterized with the rate capability analysis (Table 2) by discharging up to 5C. The corresponding battery showed a quite normal behavior, so discharging lesser capacity at higher C-rates, and at 5C a small amount of capacity (~24 mAh·g^{-1}) could be discharged in the CC-phase. The remaining capacity discharged in the cycle is discharged in the CV-phase. At the end of the rate capability analysis, the cell exhibits a capacity retention of 98.7 %. Subsequently a lifetime analysis was started at which the cell is symmetrically charged/discharged 50 times at C/2, followed by 5 times at C/5 to check the remaining capacity retention of the battery. Overall, the battery endured more than 500 cycles before reaching EoL which is a quite high value for a coin cell type. When analyzing the CC-phase, it can be concluded that the EoL of the battery is indicated earlier due to a drop in CC-capacity. The new electrode architecture allows for achieving high cycle numbers at moderate charging/discharging times.

Post-mortem analyses

The cells were disassembled after facing EoL. Directly after the disassembling no electrode or material delamination could be observed which could be proven by SEM (Figure 5b). Additionally, SEM analyses were conducted on sections of both new and used electrodes (Figure 5).
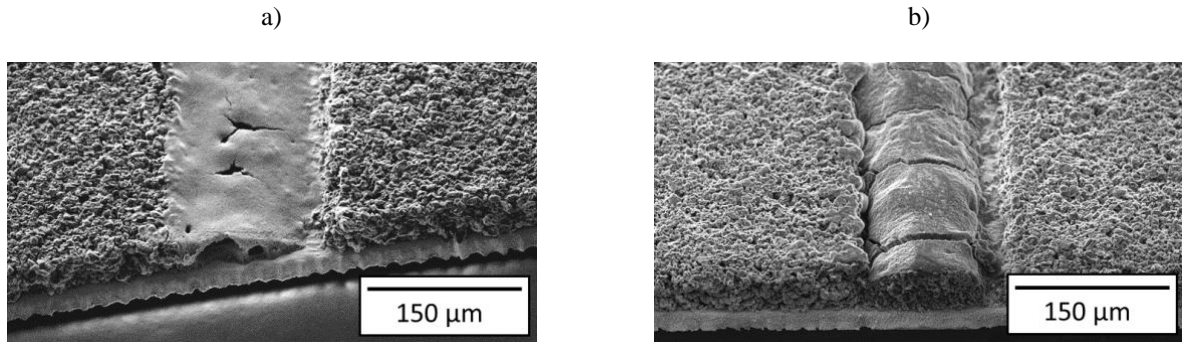
Figure 5: SEM of a) the SaA-electrode after printing and b) a SaA-electrode after facing end-of-life (after cycling). The images were made by using a secondary electron (SE) detector.

In Figure 5a, the as-printed electrode shows that the printed silicon paste is present in the structure, but there are also some cracks and cavities. It is expected that these defects are caused by the drying of the electrode and so the shrinkage of the printed paste. Regarding the cycled electrode in (Figure 5b) it can be seen that there are cracks in the silicon region of the electrode oriented transversely to the groove direction. It can be concluded by comparing the SEM images that the material has undergone a volume change during electrochemical cycle. Additionally, no loss of active material due to delamination during cycling was detected. It can therefore be stated that although large cracks can be detected using SEM, the electrode still appears to be intact overall.

Additionally, to the SEM the SaA-electrodes were characterized at their EoL by LIBS. The received LIBS signal was analyzed regarding the qualitative lithium concentration and the corresponding data are displayed in Figure 6.
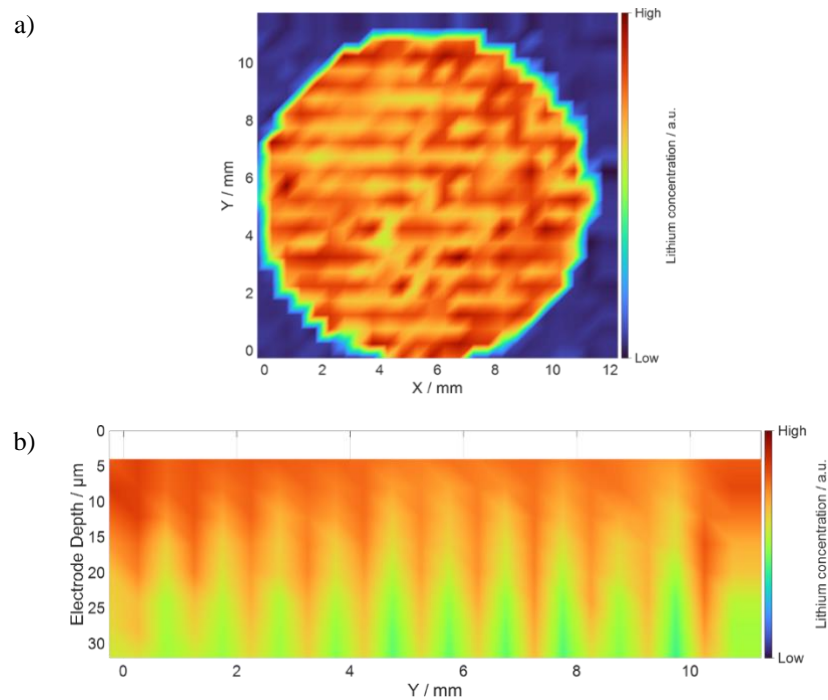

Figure 6: Lithium elemental mapping of the SaA-electrode at EoL. The LIBS data were analyzed with regard to the qualitative lithium concentration by dividing the intensity of the lithium peak by the overall intensity of the measurement. The data was visualize with MatLab (ver. 2021b): a) top view of the 4th measured layer of the electrode and b) average value of the horizontal measured values by including only the measured values of the electrode area.

Figure 6a shows a top view of the 4th measured LIBS layer of the electrode. Here, the round shape of the electrode is recognized in the data. The observed elemental line pattern, in which more lithium is measured, corresponds to the grooves

in which the silicon-rich paste was printed. The amount of lithium in the silicon-rich grooves is increased by a factor of 1.17 in comparison to the amount of lithium in graphite segments. The data displayed in Figure 6b are average values (in x- direction) which were calculated from each measured LIBS layer by including only the electrode area. The diagram shows that there is more lithium detected at the top of the electrode than in deeper regions. Such lithium gradients arise due to the tortuosity of the electrode and thus different kinetics of Li diffusion processes. However, the channels printed with silicon-rich paste exhibit an increased concentration of Li from the surface down to the current collector. This is due to the different Li-ion diffusion kinetics and the varying amount of Li stored in silicon and graphite. In comparison to the Si segments, the graphite segments are delithiated more quickly due to a smaller amount of stored Li and a larger diffusion coefficient. Thus, the cross-sectional Li elemental mapping (Figure 6b) illustrates a slight delay in the release of Li in the Si layers. In addition, the LIBS measurement reveals that no inactive areas or electrode lift-off could be detected.

4. CONCLUSION & OUTLOOK

This study reported about the development of a silicon-rich paste for LIFT. The printed electrodes were electrochemically characterized in coin cells versus lithium. After electrochemical priming, the electrodes have a high specific capacity of 3029 mAh·g^{-1}. However, the 2D Si anodes undergo an expected huge capacity fading during cycling at low currents of C/10. To achieve a higher cyclability, a new electrode architecture was established. For this purpose, a conventional coated composite graphite electrode was used as base anode. Via ultrafast laser ablation, a groove structure pattern with a pitch of 1 mm was realized. The grooves were then partially filled with a silicon-rich paste using positioned printing via LIFT. The electrode design with the graphite and silicon segments was chosen to reduce possible compressive stresses caused by lithiated silicon on the graphite areas during the electrochemical cycles. Additionally, it is assumed that the stable graphite surrounding the printed silicon provides mechanical anchoring and adhesion, which positively impacts overall adhesion. The overall silicon content is calculated to be 5.7 wt.%. The cells with the designed electrodes were first cycled with electric currents up to 5C and show good performance. Subsequently, a lifetime analysis was performed with 50 cycles at a C-rate of C/2 followed by 5 cycles at a C-rate of C/5. Overall, the cell achieved a long lifetime with over 500 cycles before reaching EoL. Afterwards the cells were disassembled and no delamination of the electrode material to the current collector was observed. The analyses via SEM and LIBS did not reveal any obvious defects in the electrode. In ongoing studies, the impact of film thickness, groove widths, and pitch on cycling performance has to be studied in more detail for identifying the most promising electrode architecture with high mass loading (>6mAh/cm^2) which finally will be transferred to large electrode footprint in high energy cells.

ACKNOWLEDGEMENT

REFERENCES

[1] W. Pfleging, *Int. J. Extreme Manuf.*, **2021,** *Vol. 1*, p. 12002 – 12022. DOI: 10.1088/2631-7990/abca84.

[2] A. Meyer, F. Ball, W. Pfleging, *Nanomaterials (Basel, Switzerland)*, **2021,** *Vol. 12*, p. 3448 – 3473. DOI: 10.3390/nano11123448.

[3] J. B. Habedank, J. Endres, P. Schmitz, M. F. Zaeh, H. P. Huber, *J. Laser Appl.*, **2018,** *Vol. 3*, p. 32205 – 32212. DOI: 10.2351/1.5040611.

[4] M. K. Majeed, R. Iqbal, A. Hussain, M. U. Majeed, M. Z. Ashfaq, M. Ahmad, S. Rauf, A. Saleem, *Crit. Rev. Solid State Mater. Sci.*, **2023**, p. 1 – 33. DOI: 10.1080/10408436.2023.2169658.

[5] C. C. Nguyen, T. Yoon, D. M. Seo, P. Guduru, B. L. Lucht, *ACS applied materials & interfaces*, **2016,** *Vol. 19*, p. 12211 – 12220. DOI: 10.1021/acsami.6b03357.

[6] A. Baasner, F. Reuter, M. Seidel, A. Krause, E. Pflug, P. Härtel, S. Dörfler, T. Abendroth, H. Althues, S. Kaskel, *J. Electrochem. Soc.*, **2020,** *Vol. 2*, p. 20516 – 20527. DOI: 10.1149/1945-7111/ab68d7.

[7] W. Pfleging, *Nanophotonics*, **2018,** *Vol. 3*, p. 549 – 573. DOI: 10.1515/nanoph-2017-0044.

[8]   H. Kim, T. E. Sutto, J. Proell, R. Kohler, W. Pfleging, A. Piqué, in *Laser-based Micro- and Nanoprocessing VIII*, SPIE Proceedings (Eds: U. Klotzbach, K. Washio, C. B. Arnold), SPIE, **2014**, p. 89680L. DOI: 10.1117/12.2037287.

[9]   P. Smyrek, H. Kim, Y. Zheng, H. J. Seifert, A. Piqué, W. Pfleging, in *Laser 3D Manufacturing III*, SPIE Proceedings (Eds: B. Gu, H. Helvajian, A. Piqué), SPIE, **2016**, *Vol. 9738*, p. 9738061 - 9738065. DOI: 10.1117/12.2211546.

[10] U. Rist, A. Reif, W. Pfleging, in *Laser-based Micro- and Nanoprocessing XVI* (Eds: R. Kling, A. Watanabe), SPIE, **2022**, *Vol. 11989*, p. 119890C1–119890C10. DOI: 10.1117/12.2609588. ISBN: 9781510648494.

[11] U. Rist, F. Ball, W. Pfleging, in *Laser-based Micro- and Nanoprocessing XVII* (Eds: R. Kling, W. Pfleging, A. Watanabe), SPIE, **2023 - 2023**, p. 28. DOI: 10.1117/12.2650281. ISBN: 9781510659230.

[12] U. Rist, V. Falkowski, W. Pfleging, *Nanomaterials (Basel, Switzerland)*, **2023,** *Vol. 17*. DOI: 10.3390/nano13172411.

[13] B. Koo, H. Kim, Y. Cho, K. T. Lee, N.-S. Choi, J. Cho, *Angew. Chem.*, **2012,** *Vol. 35*, p. 8892 – 8897. DOI: 10.1002/ange.201201568.

[14] A. Magasinski, B. Zdyrko, I. Kovalenko, B. Hertzberg, R. Burtovyy, C. F. Huebner, T. F. Fuller, I. Luzinov, G. Yushin, *ACS applied materials & interfaces*, **2010,** *Vol. 11*, p. 3004 – 3010. DOI: 10.1021/am100871y.

[15] N. P. W. Pieczonka, V. Borgel, B. Ziv, N. Leifer, V. Dargel, D. Aurbach, J.-H. Kim, Z. Liu, X. Huang, S. A. Krachkovskiy, G. R. Goward, I. Halalay, B. R. Powell, A. Manthiram, *Adv. Energy Mater.*, **2015,** *Vol. 23*, p. 1501008 – 1501017. DOI: 10.1002/aenm.201501008.

[16] H. Bin, I. A. Shkrob, S. Zhang, L. Zhang, J. Zhang, C. Liao, Z. Zhang, W. Lu, L. Zhang, *J. Power Sources*, **2018**, p. 671 – 676. DOI: 10.1016/j.jpowsour.2017.12.068.

[17] Y.-M. Zhao, F.-S. Yue, S.-C. Li, Y. Zhang, Z.-R. Tian, Q. Xu, S. Xin, Y.-G. Guo, *InfoMat*, **2021,** *Vol. 5*, p. 460 – 501. DOI: 10.1002/inf2.12185.

[18] Juan M. Fernández-Pradas, in *Laser Printing of Functional Materials: Electronics, 3D Microfabrication and Biomedicine* (Eds: A. Pique´, P. Serra), John Wiley & Sons Incorporated. Newark, **2018**, p. 63–89. ISBN: 978-3-527-34212-9.

[19] J. Kumberg, M. Müller, R. Diehm, S. Spiegel, C. Wachsmann, W. Bauer, P. Scharfer, W. Schabel, *Energy Technol.*, **2019,** *Vol. 11*, p. 1900722. DOI: 10.1002/ente.201900722.

[20] W. Pfleging, Y. Zheng, in *Laser-based Micro- and Nanoprocessing XVI* (Eds: R. Kling, A. Watanabe), SPIE, **2022**, p. 22. DOI: 10.1117/12.2609781. ISBN: 9781510648494.

[21] L. Haneke, F. Pfeiffer, P. Bärmann, J. Wrogemann, C. Peschel, J. Neumann, F. Kux, S. Nowak, M. Winter, T. Placke, *Small (Weinheim an der Bergstrasse, Germany)*, **2022**, p. e2206092. DOI: 10.1002/smll.202206092.

[22] Z. Yang, S. E. Trask, X. Wu, B. J. Ingram, *Batteries*, **2023,** *Vol. 2*, p. 138. DOI: 10.3390/batteries9020138.

[23] H. Wu, Y. Cui, *Nano Today*, **2012,** *Vol. 5*, p. 414 – 429. DOI: 10.1016/j.nantod.2012.08.004.

[24] H. Shi, X. Liu, R. Wu, Y. Zheng, Y. Li, X. Cheng, W. Pfleging, Y. Zhang, *Applied Sciences*, **2019,** *Vol. 5*, p. 956 – 964. DOI: 10.3390/app9050956.

[25] R. Kasinathan, M. Marinaro, P. Axmann, M. Wohlfahrt-Mehrens, *Energy technology (Weinheim, Germany)*, **2018,** *Vol. 11*, p. 2256 – 2263. DOI: 10.1002/ente.201800302.

[26] Y. Zheng, H. J. Seifert, H. Shi, Y. Zhang, C. Kübel, W. Pfleging, *Electrochim. Acta*, **2019**, p. 502 – 508. DOI: 10.1016/j.electacta.2019.05.064.